

Abstract:

Bacterial nanowires have garnered recent interest as a proposed Extracellular Electron Transfer (EET) pathway that links the bacterial electron transport chain to solid-phase electron acceptors away from the cell. *In vivo* fluorescence Light Microscopy (fLM) imaging recently showed that *Shewanella oneidensis* MR-1 nanowires are extensions of the outer membrane that contain EET components. However, their fine structure and distribution of cytochrome electron carriers remained unclear, making it difficult to evaluate the electron transport mechanism along the nanowires. Here, we report high-resolution images of nanowires using Electron Cryo-Tomography (ECT). We developed a robust method for fLM imaging of nanowire growth on electron microscopy grids and used correlative light and electron microscopy to identify and image the same nanowires by ECT. Our results confirm that *S. oneidensis* nanowires are outer membrane extensions, and further reveal that nanowires are dynamic chains of interconnected Outer Membrane Vesicles (OMVs) with variable dimensions, curvature, and extent of tubulation. Junction densities that potentially stabilize OMV chains are seen between neighboring vesicles in cryotomograms. Our ECT results also provide the first hints of the positions and packing of periplasmic and outer membrane proteins consistent with cytochromes. We observe tight packing of putative cytochromes along lateral patches that extend tens of nanometers, but not across the micrometer scale of whole nanowires. We therefore propose that electron transfer along nanowires involves a combination of direct hopping and diffusive events that link neighboring redox proteins.

Introduction

Redox reactions are essential to all biological energy conversion strategies¹. In respiratory organisms, free energy is harvested from the environment as electrons extracted from an electron donor (fuel) are transferred through the cellular electron transport chain to a terminal electron acceptor (oxidant). While most eukaryotes, including humans, are dependent on molecular oxygen (O₂) as their terminal electron acceptor, anaerobic prokaryotes can acquire energy by employing a wide variety of alternative Electron Acceptors (EAs). Like O₂, many of these EAs can diffuse inside the cell, where they participate in redox reactions with intracellular electron transport chain components. However, Dissimilatory Metal-Reducing Bacteria (DMRB) can also utilize insoluble EAs such as metal oxide minerals, to which the cellular membrane is impermeable, by transporting electrons across the cell envelope²⁻⁵. This Extracellular Electron Transport (EET) process has important implications in renewable energy technologies, wastewater treatment, bioremediation, and global biogeochemical cycles^{3,6-8}.

The Gram-negative bacterium *Shewanella oneidensis* MR-1 is the best-characterized DMRB model system^{2,5,9,10}. Previous electrochemical, biochemical, genetic, and structural studies of *Shewanella* have identified an intricate network of redox proteins that traffic electrons from the inner membrane quinone pool through the periplasm and across the outer membrane^{6,10,11}. A critical electron transfer module is the Mtr pathway, in which electrons are transferred from the periplasmic decaheme

cytochrome MtrA to the outer membrane decaheme cytochrome MtrC through the transmembrane porin MtrB^{12,13}. Under conditions of direct cell surface contact with minerals or electrodes, MtrC (and a partnering decaheme cytochrome OmcA) can transfer electrons directly to these solid EAs¹⁴. The EET rate from the surface-exposed cytochromes to such external surfaces can also be enhanced by interactions with secreted flavins that function either as cytochrome-bound cofactors¹⁵⁻¹⁷ or soluble shuttles capable of interacting with even more distant EA surfaces^{18,19}. The *Shewanella* multiheme cytochromes MtrC and OmcA have also been found to localize along conductive outer membrane extensions known as bacterial nanowires, which are associated with Outer Membrane Vesicles (OMVs)²⁰⁻²². Nanowires may offer a pathway for extending the respiratory electron transport chain of cells up to micrometers away from the inner membrane, possibly even to other cells²².

Despite the potential impact in understanding cell-cell interactions, as well as for enhancing electron transfer at the biotic-abiotic interface in renewable energy technologies, we still lack a detailed understanding of the structure and electron transport mechanism of *S. oneidensis* nanowires. Physical measurements of conductance along the nanowires have revealed the importance of cytochromes as the charge carriers, but the measurements were made on dried samples so the distribution and conformation of the electron transport components may not be the same as *in vivo*²¹. Fluorescence-based *in vivo* techniques recently showed that *S. oneidensis* nanowires are extensions of the outer membrane and periplasm, and that nanowire production correlates with increased cellular respiration²². Additionally, immunolabeling experiments confirmed the localization of multiheme outer membrane cytochromes along the nanowire length²². However, the

diffraction-limited resolution precluded visualization of the macromolecular details of the nanowire structure²². Many other details remain unclear, including formation and stabilization mechanisms, cytochrome distribution, as well as the processes underlying the large morphological variation and dynamic nature of these filaments. One particular difficulty in previous studies is distinguishing nanowires from other filaments (flagella, pili, and dehydrated extracellular polymeric substances (EPS))^{23,24}. Electron Cryo-Tomography (ECT), by contrast, can deliver high-resolution three-dimensional structural details of cellular structures. By capturing the specimen in a thin layer of vitreous ice, structures of interest are preserved in a fully-hydrated and essentially native state²⁵.

Here we use ECT to capture the highest resolution images of bacterial nanowires to date. We have developed a novel experimental set-up allowing bacteria to form nanowires on an EM grid inside a perfusion flow imaging platform. Using fluorescent membrane staining, we monitored nanowire growth in real-time by live fluorescence Light Microscopy (fLM) and subsequently located and imaged the same nanowires by ECT. We discuss the challenges involved in retaining the fragile nanowire structures for EM imaging, and the methodology we developed to address these sample preparation issues. Our fLM and ECT results reveal the vesicular nature of *S. oneidensis* nanowires and shed light on a potential mechanism for their stabilization as OMV chains. The high resolution of ECT reveals the positions of the putative periplasmic and outer membrane multiheme cytochromes under near-native conditions. We discuss how these structural measurements inform and help refine proposed models^{22,26,27} for electron transport physics in *S. oneidensis* nanowires.

Results

Conditions for Reliable Nanowire Production for ECT

While OMVs and bacterial nanowires have previously been described in both planktonic and surface-attached *Shewanella* cultures using various methods such as EM, Atomic Force Microscopy (AFM), and fLM^{20-22,28}, there has not been an extensive exploration of the optimal culturing and sample preparation workflows most suitable for detection of these structures. Here we utilized negative stain Transmission Electron Microscopy (TEM) and ECT to assess both culturing and sample preparation steps that lead to robust formation and preservation of nanowires.

We first tested liquid cultures of *S. oneidensis* MR-1, either from continuous flow bioreactors (chemostats) operated under electron acceptor-limited conditions that trigger nanowire formation²⁰⁻²², or from sealed serum bottles where *S. oneidensis* cells underwent a transition to electron acceptor limitation as they gradually consumed the available dissolved oxygen supplied from the headspace (Materials and Methods). Samples from both chemostats and serum bottles, either unfixed or fixed with glutaraldehyde, were visually assayed for nanowire formation by EM. Surprisingly, even in fixed cells, nanowires were rarely detected by either negative stain TEM or ECT, despite the presence of membrane blebs and OMVs (Figs. S1, S2). By contrast, similar to previous reports²³, we observed an abundance of filaments by Scanning Electron Microscopy (SEM) imaging of our liquid culture samples (data not shown). However, our investigations revealed that not all filaments observed in SEM could be identified as nanowires (additional experiments in progress), highlighting the need for improved

methodology and care in interpretation of imaging results to distinguish nanowires from pili, flagella, and filamentous polymeric substances²⁴.

Because nanowires in liquid cultures were only rarely observed by both ECT and negative stain TEM, we next tested surface-attached cultures. Building on our previous work utilizing surface-attached cultures to reveal the composition of *S. oneidensis* nanowires²², we developed a method for monitoring nanowire growth on EM grids inside a perfusion flow imaging platform by fLM (Fig.1). While nanowires were seen in this set-up by fLM, we observed only very few intact nanowires by either negative stain TEM or ECT, in unfixed or formaldehyde-fixed samples from this set-up (S3, S4). This suggests that nanowires are fragile structures. Fortunately, fixation with glutaraldehyde stabilized the nanowires, enabling us to reliably visualize the structures by Correlative Light and Electron Microscopy (CLEM) (Fig. S5, Movies S1 and S2). We conclude that nanowires are more frequent and consistently present in surface-attached cultures, but comparatively uncommon in liquid cultures under our experimental conditions.

Live Fluorescence Microscopy of Nanowire Growth on EM Grids

Our optimized perfusion flow imaging platform set-up consists of a microliter-volume laminar perfusion flow chamber placed on an inverted fluorescence microscope, where an EM grid-attached glass coverslip seals the chamber (Fig. 1). *S. oneidensis* cells are then introduced into the chamber, where they attach to the surface of the EM grid, and sterile media is flowed into the chamber throughout the experiment. The laminar Poiseuille flow (no mixing from upper layers), combined with negligible flow speed at

the surface-solution interface (no-slip condition), where the cells are located, results in O₂-limiting conditions that trigger nanowire formation directly on the EM grid²².

Using this set-up, we observed the formation of nanowires live on the EM grid surface with the fluorescent membrane dye FM 4-64FX. Cells were located relative to grid holes by fLM (Fig. 2 and Movie S3) to allow registration with subsequent EM imaging. It has been shown previously that the conductance of nanowires depends on the presence of the outer membrane multiheme cytochromes MtrC and OmcA²¹, and these cytochromes have been detected using immunofluorescence along membrane-stained nanowires from perfusion flow cultures²², so the nanowires we observe are likely conductive.

Nanowires are Dynamic Chains of Interconnected OMVs Stabilized by Junction Densities

For ECT, grids from the perfusion flow imaging platform were removed, plunge-frozen and transferred to the electron microscope, where the fLM-identified nanowires were located and imaged (Fig. 3). ECT images confirmed that nanowires are outer membrane extensions, with the two leaflets of the lipid bilayer clearly resolved along their length (Fig. 4A-B). Cryotomograms revealed nanowires to be chains of interconnected OMVs in both unfixed (Fig. 4C) and fixed samples (Fig. 4D-G). Previous fLM and AFM work showed that nanowires cover a range of morphologies from apparently smooth tubular extensions to clearly distinguishable OMV chains²². Here, we observed that, with the exception of one smooth filament (Fig. S6), all nanowires including those that appeared smooth in fLM were, at high resolution, distinguishable as OMV chains (Figs. 3 and 4). The images also captured vesicle budding (Fig. 4B), a

process that underlies the initial stage of OMV production²⁹. Importantly, ECT also allowed us to clearly distinguish between pili, flagella and nanowires – the three known extracellular appendages in *S. oneidensis* (Fig. 4D-G, Movies S4 and S5).

Electron-dense regions were observed at the junctions connecting neighboring vesicles throughout the length of the nanowires in both fixed and unfixed samples (Figs. 5A, S7 and Movie S6). This finding points to yet unknown molecules that potentially facilitate the constriction of the membrane to allow OMV connections, and is consistent with the fLM observations of the nanowires as dynamic structures capable of growth, retraction, and reversible transition between OMV chain and individual vesicle morphologies (Figs. 5B, 5C, and Movies S7, S8, S9, S10).

ECT Reveals the Distribution of Periplasmic and Outer Membrane Proteins Consistent with Multiheme Cytochromes

The outer membrane cytochromes MtrC and OmcA have been shown to localize along the nanowire length²² and are essential for solid-state conductance of nanowires in *S. oneidensis*^{21,22}. The packing density of these cytochromes is crucial in determining the mechanism of electron transport along nanowires, but has remained unknown. Here, using ECT, we observe electron-dense particles on the interior and exterior of the nanowires' membrane consistent with periplasmic and outer membrane cytochromes (Fig. 6A). Fig. 6B overlays available structures of the decaheme cytochromes MtrA³⁰ and MtrC¹⁶ on representative interior and exterior densities, respectively, highlighting the similarity in overall shape and size of these structures to the observed EM densities. From the cryotomograms, it is possible to represent all the observed interior and exterior

densities as model points and reconstruct 3-dimensional isosurfaces that represent both the nanowire structure and the putative EET proteins (Fig. 6C and Movie S11). While we observed sections up to ~70 nm and ~75 nm where the exterior and interior densities clustered closely with 7.3 nm (SD=2.1 nm) and 8.9 nm (SD=2.0 nm) center-to-center distances, respectively (Fig. 6D-E), we did not observe a continuous crystalline-like packing of these densities along the entire nanowire length (Fig. 6H). Instead, the outer membrane and periplasmic densities were distributed over a range of center-to-center spacings, from 4.9 to 32.5 nm and 5.0 to 29.0 nm, respectively (Fig. 6I).

Discussion

Here we show high-resolution images of nanowires in *S. oneidensis* using electron cryo-tomography. We found nanowires to be OMV chains possibly stabilized by constriction densities at the junctions. Bacterial membrane extensions have been reported in multiple organisms: ‘Nanopods’ in *Comamonadaceae* including *Delftia*³¹, ‘outer membrane tubes’ in *Francisella novicida*³², ‘periplasmic tubules’ in *Chlorochromatium aggregatum*³³, ‘membrane tubules’ in *Salmonella typhimurium*³⁴, ‘nanotubes’ connecting *Escherichia coli* cells to each other and to *Acinetobacter baylyi* cells³⁵, and ‘connecting structures’ that allow exchange of material between *Clostridium acetobutylicum* and *Desulfovibrio vulgaris* cells³⁶. However, membrane extensions in the form of OMV chains have only recently been discovered and much remains unknown about their formation mechanism and specific function³⁷. In the Gram-negative *Shewanella vesiculosa*³⁸ and *Myxococcus xanthus*^{39,40} and the Gram-positive *Bacillus subtilis*⁴¹, membrane extensions in the form of OMV chains, similar to those reported here, have

been observed using cryo-EM with implications for cell-cell connections in the latter two examples. While the *S. oneidensis* nanowires are thought to function as electron conduits²¹, their structural similarity to these previous reports highlights the significance of imaging nanowires as a model system to study the formation of OMV chains.

In order to find a condition that consistently and frequently produced intact nanowires for ECT imaging, we systematically tested different methods of growth and sample preparation conditions, as summarized in Fig S8. Using surface-attached cultures fixed with glutaraldehyde stabilized the nanowires, enabling us to record high-resolution cryotomograms of a number of *S. oneidensis* nanowires as shown in Fig 4. The OMV chain morphology exhibited by these nanowires is unlikely to be an artifact of fixation since we also observed a similar OMV chain architecture in nanowires from unfixed samples (Figs 6A, S4). While flagella and pili were identified as smooth filaments that measured ~10 and ~3 nm in thickness, respectively, nanowires varied in thickness typically from ~20 to 170 nm (Fig. 4D-G), depending on the size and extent of tubulation of the constituent OMVs. This is in contrast to previously reported AFM measurements of ~10 nm for air-dried nanowires. This discrepancy arises from the difference in sample preparation between the two methods. While in AFM dehydration causes nanowires to collapse to an ~10 nm thickness, roughly corresponding to two lipid bilayers, ECT preserves samples in a hydrated near-native state, leading to more accurate estimates of nanowire thickness. An interesting feature we observed is the ability of the vesicle chains to branch (Figs. 6A, S9 and Movie S12), which may offer the advantage of increasing the likelihood of contacting terminal solid-phase electron acceptors in the environment. To our knowledge this is the first report of branching observed in bacterial membrane

extensions. Nanowires were also found to be flexible (Fig S10), potentially improving their ability to contact solid-phase EAs.

Our ECT images of *S. oneidensis* nanowires reveal that individual vesicles open into each other, share a continuous lumen, and thus form a chain of vesicles that are internally connected. This OMV architecture is reminiscent of the “pearls on a string” morphology caused by the pearling instability that transforms membrane tubes into a string of interconnected vesicles^{42,43}. The transformation may be caused by an increase in membrane tension that can be stimulated in multiple ways, including osmotic gradient⁴⁴, mechanical perturbation^{42,43}, elongational flow⁴⁵, electric field⁴⁶, bilayer asymmetry⁴⁷, nanoparticle adsorption onto the inner leaflet⁴⁸, or polymer anchorage onto a membrane^{49,50}. Our observation of densities at the junctions of neighboring vesicles in both fixed (Fig. 5A and Movie S6) and unfixed (Fig. S7) nanowires is consistent with the latter mechanism of polymer anchorage onto a membrane in which ‘constriction densities’ or ‘junction densities’ interact with the nanowire membrane, resulting in the formation of the OMV morphology (Fig 5A arrows). As schematized in Fig. 5D, addition and removal of such constriction densities may also explain the dynamic behavior exhibited by nanowires, where long nanowires transition to and from individual vesicles (Fig. 5B-C, Movies S7, S8, S9, S10).

The solid-state conductance of *S. oneidensis* nanowires has been linked to the presence of the outer membrane decaheme cytochromes MtrC and OmcA²¹. These cytochromes are localized along the length of *S. oneidensis* nanowires and are thought to mediate electron transport by a multistep redox hopping mechanism^{22,26}. While the intra-protein hemes’ arrangement within MtrC and OmcA allows sequential tunneling

(hopping) through the heme chain^{51,52}, the packing density and orientation of these cytochromes are critical parameters that determine the mechanism of putative inter-protein electron transfer along the entire nanowire. However, prior to this work, little was known about the packing density of MtrC and OmcA molecules along nanowires.

The nanowires in ECT showed densities both on the inside and outside of the membrane (Fig. 6A), features consistent with the periplasmic and outer membrane proteins, respectively, and as expected from immunofluorescence measurements²². To determine whether the outside densities match the size of MtrC, we overlaid the crystal structure of MtrC¹⁶ onto three of these densities, as illustrated in Figure 6B. Since these densities did not appear symmetric on the EM map, and since the orientation of MtrC at the cellular outer membrane is unknown, we overlaid the MtrC crystal structure in the orientation that best matched each density. Using this approach, the size of the outer membrane features was found to be consistent with MtrC. This approach cannot distinguish between MtrC and other *Shewanella* outer membrane decaheme cytochromes, such as MtrF and OmcA, all of which have substantial structural homology¹⁶. The size of these proteins is at the resolution limit of tomography and additional experiments are needed to obtain further details about the interaction and association of MtrC with other proteins in the MtrCAB complex^{13,53} that is proposed to form a contiguous EET conduit from the periplasm to the cellular exterior. We applied a similar approach to compare the interior nanowire densities with the periplasmic decaheme cytochrome MtrA. The interior densities were more oblong than their outside counterparts, an observation consistent with the rod-like shape of MtrA previously revealed by Small-Angle X-ray Scattering (SAXS)³⁰. By overlaying this low-resolution SAXS model on the EM map, the

internal densities were found to be consistent in size and shape with MtrA (Fig. 6B). While the structure of MtrB is not yet known, we overlaid the crystal structure of a similarly-sized protein (LptD from *Salmonella enterica*⁵⁴⁵⁵) in Figure 6B, and found that the size of the porin matches the width of the bilayer as expected. Taken collectively, our analyses highlight the similarity in overall shape and size between multiheme cytochromes and the observed EM densities.

The isosurface representation of the nanowires, including the placement of the detected periplasmic and outer membrane proteins (Fig. 6C and Movie S11), allows a holistic evaluation of different inter-protein electron transfer mechanisms. Remarkably, we observed outer membrane (Fig. 6D) and periplasmic (Fig. 6E) proteins clustering closely over segments of the nanowire. The center-to-center distances between neighboring proteins within the tightest-packed segments were 7.3 nm (SD=2.1 nm) and 8.9 nm (SD=2.0 nm) for the outer membrane and periplasmic proteins, respectively. Taking the overall dimensions of MtrC¹⁶ (~9×6×4 nm) and the locations of the hemes (including terminal hemes at the protein edges) into account¹⁶, the center-to-center distances point to the possibility of direct electron tunneling (requiring < 2 nm separation¹) between terminal hemes of neighboring outer membrane cytochromes within segments. However, such a crystalline-like packing of cytochromes was not observed over the micrometer lengths of whole wires (Fig. 6). Instead, we observed a wide distribution of center-to-center spacings, presented for both the periplasmic and outer membrane densities in Fig. 6I. Since center-to-center spacings beyond 11 nm and 7 nm for MtrC and MtrA, respectively, do not allow direct electron transfer between

neighboring cytochromes (see Materials and Methods), intermediate diffusive events are required to link the hemes of neighboring proteins beyond such distances.

This may be accomplished by lateral diffusion of the multiheme cytochromes, resulting in collisions and electron exchange between neighboring cytochromes. For example, Paquette *et al.*⁵⁶ suggested that OmcA, which interacts with MtrC and is attached only by a lipidated cysteine at the N-terminus, is mobile on the surface of *Shewanella*. Using $3 \mu\text{m}^2/\text{s}$ as a representative value for the diffusion coefficient of integral membrane proteins of similar size⁵⁷, the median inter-cytochrome distance can be traversed in 10^{-5} s (Table S1, Materials and Methods), a time scale comparable with the electron residence time in the heme chains of the individual cytochromes, estimated from calculated and measured electron flux through MtrF (10^4 s^{-1})^{51,52} and MtrCAB¹⁴. In addition, the electron transfer rate can be enhanced by diffusion of redox active molecules between cytochromes. In this context, it is important to note that the *Shewanella* decaheme cytochromes have flavin binding sites¹⁶, and flavins are known to enhance EET¹⁷. The precise values of the diffusion coefficients (MtrC/OmcA proteins in the membrane, the likely faster MtrA diffusion within the periplasm, and the effect of crowding) are unknown. The preceding analysis is therefore intended for heuristic reasons, and to motivate future studies targeting the diffusive dynamics of electron carriers in bacterial nanowires. In summary, our ECT imaging revealed particles consistent in size and morphology with decaheme cytochromes and their distribution along nanowires. Although we do not yet know whether all of the densities observed on the inside and the outside of the membrane correspond to MtrA and MtrC respectively (since we cannot distinguish between MtrC and other structural homologs, such as MtrF

and OmcA, and there may be other membrane proteins as well), it is already clear that cytochromes are not tightly packed along the entire length of the nanowire. This irregular packing of cytochromes means that EET along whole nanowires likely involves a combination of direct electron transfer within segments of closely packed cytochromes and cytochrome diffusion to bridge larger length scales.

Acknowledgements

We thank Drs. Yi-Wei Chang and Matthew Swulius for help preparing Figures 6B and 6C, respectively. We are grateful to Dr. Sean J. Elliott for providing the SAXS model file for MtrA³⁰ used in Figure 6B. Thanks to Dr. Catherine Oikonomou for helping edit the manuscript. P.S. acknowledges support by the Caltech Center for Environmental Microbial Interactions (CEMI). Work in the laboratory of G.J.J. is supported by the Howard Hughes Medical Institute. The *in vivo* nanowire imaging platform and mapping of EET proteins is funded by Air Force Office of Scientific Research PECASE award FA955014-1-0294 to M.Y.E-N. Modeling of ET kinetics and partial support for S.P. are funded by the Division of Chemical Sciences, Geosciences, and Biosciences, Office of Basic Energy Sciences of the US Department of Energy through grant DE-FG02-13ER16415 to M.Y.E-N.

Materials and Methods

Chemostat Growth Conditions

S. oneidensis MR-1 cells were grown in continuous flow bioreactors (BioFlo 110; New Brunswick Scientific) with an operating liquid volume of 1 L, as previously described²⁰⁻

²². 5 mL of a stationary-phase overnight Luria-Bertani (LB) culture was injected into the bioreactor, while Dissolved Oxygen Tension (DOT) was maintained at 20% by adjusting the ratio of N₂/air mixture entering the reactor (using automatic mode). After 20 hours, and as the culture reached stationary phase, continuous flow of the medium was started with a dilution rate of 0.05 h⁻¹ while DOT was still maintained at 20%. After 48 hours of aerobic growth under continuous flow conditions, the DOT was manually reduced to 0% by adjusting the N₂/air mixture entering the reactor. O₂ served as the sole terminal electron acceptor throughout the experiment. pH was maintained at 7.0, temperature at 30 °C and agitation at 200rpm to minimize mechanical shear forces. 40 hours after DOT reached 0%, samples were taken from the chemostat for TEM imaging.

Serum Bottle Growth Conditions

S. oneidensis MR-1 was grown overnight in Luria-Bertani (LB) broth at 30 °C up to an OD₆₀₀ of 2.4-2.8. 200 µL of this overnight culture was added to each of two duplicate, sealed, and autoclaved 100-mL serum bottles containing 60 mL of a defined medium²². One of the two bottles acted as a control and was not used for imaging. To the control bottle, 5µM resazurin was added to indicate the O₂ levels in the medium. The bottles were then placed in an incubator at 30 °C, shaking at 150 rpm until the color due to resazurin in the control bottle completely faded, indicating anaerobic conditions. We then took 200 µL of sample from the bottle that did not contain resazurin for TEM imaging.

Perfusion Flow Imaging Platform

The perfusion flow imaging platform was used as described previously²², with some modifications. *S. oneidensis* MR-1 was grown overnight in Luria-Bertani (LB) broth at 30 °C up to an OD₆₀₀ of 2.4-2.8 and washed twice in a defined medium²². A glow-discharged, X-thick carbon-coated, R2/2, Au NH2 London finder Quantifoil EM grid (Quantifoil Micro Tools) was glued to a 43 mm × 50 mm No. 1 glass coverslip using waterproof silicone glue (General Electric Company), applied to two opposite edges of the grid, and let dry for ~30 min. Using a vacuum line, the perfusion chamber (C&L Instruments, model VC-LFR-25) was sealed against the grid-attached glass coverslip and placed on an inverted microscope (Nikon Eclipse Ti-E) that continually imaged the grid surface. ~10 ml of the washed culture was injected into the chamber slowly to allow cells to settle on the grid surface, followed by flow of sterile defined medium from an inverted serum bottle through a bubble trap (Omnifit, model 006BT-HF) into the perfusion chamber inlet. The serum bottle was pressurized by N₂ in the headspace to sustain a flow rate of 5±1 µL/s. After ~2 hrs of perfusion flow, cells on the grid surface began to produce nanowires. Cells and nanowires were visualized by the fluorescent membrane stain FM 4-64FX that was present in the flow medium throughout the experiment (25 µg in 100 mL of medium). Subsequently, the flow of medium was stopped and the perfusion chamber was opened under sterile medium. If fixed, the sample (cells on EM grid-attached coverslip) was treated with either 2.5% glutaraldehyde for 15 min or 4% formaldehyde for 60 min. The grid was then detached from the coverslip by scraping off the silicone glue at the grid edges using a 22G needle, and rinsed by transferring 3 times in deionized water, before using for TEM imaging.

Negative Stain Transmission Electron Microscopy (TEM)

(i) Chemostat: Samples taken from the chemostat were immediately fixed with 2.5% glutaraldehyde and stored at 4 °C. 2ul of this fixed sample was spotted on a glow-discharged, X-thick carbon-coated, R2/2, Au NH₂ London finder Quantifoil EM grids (Quantifoil Micro Tools) and let sit for 2 min. Any remaining liquid was blotted off gently using a kimwipe and the grid was stained with 1% uranyl acetate for 2 min before gently blotting the remaining stain. The grid was then allowed to dry for a day at room temperature before imaging in TEM.

(ii) Perfusion Flow Imaging Platform: The fixed grid from the perfusion flow imaging platform was blotted to remove excess liquid, and stained with 1% uranyl acetate for 2 min before gently blotting the remaining stain. To obtain an fLM image for correlation with EM, the grid was rehydrated with deionized water and reimaged on the inverted fluorescent microscope. The grid was then blotted again and let dry at room temperature before imaging in TEM.

Electron Cryo-Tomography (ECT)

ECT samples were prepared as described previously⁵⁸ with minor modifications. Cells from serum bottles and chemostats were mixed with BSA-treated 10 nm colloidal gold solution and 4 µl of this mixture were applied to a glow-discharged, X-thick carbon-coated, R2/2, 200 mesh copper Quantifoil grid (Quantifoil Micro Tools) in a Vitrobot chamber (FEI). Excess liquid was blotted off with a blot force of 6, blot time of 3 s, and drain time of 1 s and the grid was plunge-frozen for ECT imaging. All perfusion samples were on glow-discharged, X-thick carbon-coated, R2/2, Au NH₂ London finder

Quantifoil EM grids (Quantifoil Micro Tools) and were blotted either manually or automatically using the Vitrobot after addition of 1.5 μ l gold fiducial markers. Imaging of all samples was performed on an FEI Polara 300-keV field emission gun electron microscope equipped with a Gatan image filter and K2 Summit counting electron-detector camera (Gatan). Data were collected using the UCSFtomo software⁵⁹, with each tilt series ranging from -60° to 60° in 1° increments, an underfocus of ~ 5 - 10μ m, and a cumulative electron dose of ~ 130 - $160 \text{ e}/\text{\AA}^2$ for each individual tilt series. The IMOD software package was used to calculate 3D reconstructions⁶⁰.

ECT Data Analysis and structure overlay of MtrC and MtrA on EM map

For figure (6C) and Movie S11 densities on the membrane interior and exterior were labeled with model points manually using the IMOD software. Density coordinates were extracted and used for distance calculations. The number of model points in (6C) is greater than the densities observed in (6A) since (6C) represents all the densities seen in the entire tomogram and (6A) is a slice from the tomogram that does not contain all the densities. For Figure 6B, crystal structure of MtrC was visualized and oriented using UCSF Chimera⁶¹. Adobe Photoshop was then used to overlay this crystal structure onto densities on the EM map. Surface view of MtrA was visualized using the PyMOL software⁶² and overlaid on EM densities using Adobe Photoshop.

Direct Tunneling Limit Calculation

To find whether direct tunneling is possible between the observed densities in Fig. 6A, we used the available structures of MtrC and MtrA to calculate the largest center-to-

center intermolecular distance that would allow direct tunneling. From the crystal structure, the dimensions of MtrC are $\sim 9 \times 6 \times 4$ nm¹⁶. Since the orientation of MtrC on the outer membrane is unknown, we took the largest dimension (9 nm) to calculate the direct tunneling limit. The known direct tunneling limit for the distance between the donor and acceptor redox sites in biological ET is ~ 2 nm¹. This sets the limit of direct tunneling between MtrCs at 11 nm (9 nm + 2 nm) center-to-center intermolecular distance, assuming redox sites are located at the edges of the molecule. In the case of MtrA, the known molecular dimensions are $\sim 10 \times 5 \times 2.5$ nm³⁰. From the EM map, it appears that MtrA is oriented with its long axis (10 nm) perpendicular to the outer membrane (Fig. 6B). Therefore, it is likely that any intermolecular electron tunneling between MtrAs occurs along the shorter axes (5 nm and 2.5 nm). Taking the larger of these two dimensions (5 nm), we calculate the limit of direct tunneling between MtrAs to be at 7 nm (5 nm + 2 nm) center-to-center intermolecular distance.

Diffusion Timescale Calculation

To calculate the timescale of diffusion-based electron transfer events, we consider diffusion-based collisions between cytochromes that are diffusing in the membrane. We calculate the timescale of diffusion-based collision between the two reacting particles in a two dimensional membrane using the Hardt approach⁶³:

$$\frac{1}{\tau_{total}} = \frac{1}{\tau_A} + \frac{1}{\tau_B}$$

Here, τ_{total} is the mean transit time for the reaction, τ_A is the mean time it takes a diffusing A particle to find an immobilized B particle and τ_B is the mean time it takes a

diffusing B particle to find an immobilized A particle. τ_A and τ_B can be calculated from the diffusion transit time expression in two dimensions^{63,64}:

$$\tau = \frac{b^2}{2D} \ln(b/a)$$

where b is the diffusion distance, a is the center-to-center distance between the reacting particles when reaction (in our case, electron transfer) occurs, and D is the diffusion coefficient of the diffusing particle. In cytochrome-cytochrome reactions, a was taken to be the average size of the cytochrome (6.33 nm for MtrC/OmcA, 3.75 nm for MtrA), b was taken to be the average nearest-neighbor distance found in the tomogram (Fig. 6I) (15.5 nm for putative MtrC/OmcA, 11.2 nm for putative MtrA), and D was assumed to be $\sim 3 \mu\text{m}^2/\text{s}$ for both MtrC/OmcA and MtrA⁵⁷. However, in finding the average, we excluded all the nearest-neighbor distances that lay within the direct tunneling limit (< 11 nm for MtrC/OmcA, < 7 nm for MtrA). Finally, using the above values, we calculated τ_{total} in Equation 1 for MtrC/OmcA to be 1.8×10^{-5} s and for MtrA to be 1.1×10^{-5} s.

References

- 1 Gray, H. B. & Winkler, J. R. Electron tunneling through proteins. *Q Rev Biophys* **36**, 341-372 (2003).
- 2 Myers, C. R. & Nealson, K. H. Bacterial Manganese Reduction and Growth with Manganese Oxide as the Sole Electron-Acceptor. *Science* **240**, 1319-1321 (1988).
- 3 Nealson, K. H., Belz, A. & McKee, B. Breathing metals as a way of life: geobiology in action. *Antonie Van Leeuwenhoek International Journal of General and Molecular Microbiology* **81**, 215-222 (2002).
- 4 Gralnick, J. A. & Newman, D. K. Extracellular respiration. *Mol Microbiol* **65**, 1-11 (2007).
- 5 Fredrickson, J. K. *et al.* Towards environmental systems biology of Shewanella. *Nature Reviews Microbiology* **6**, 592-603 (2008).

501 6 Bretschger, O. *et al.* Current production and metal oxide reduction by *Shewanella*
502 *oneidensis* MR-1 wild type and mutants. *Appl. Environ. Microbiol.* **73**, 7003-7012
503 (2007).
504 7 Logan, B. E. Exoelectrogenic bacteria that power microbial fuel cells. *Nat Rev*
505 *Micro* **7**, 375-381 (2009).
506 8 Rabaey, K. & Rozendal, R. A. Microbial electrosynthesis - revisiting the electrical
507 route for microbial production. *Nature Reviews Microbiology* **8**, 706-716 (2010).
508 9 Hau, H. H. & Gralnick, J. A. Ecology and biotechnology of the genus *Shewanella*.
509 *Annu Rev Microbiol* **61**, 237-258, doi:10.1146/annurev.micro.61.080706.093257
510 (2007).
511 10 Breuer, M., Rosso, K. M., Blumberger, J. & Butt, J. N. Multi-haem cytochromes
512 in *Shewanella oneidensis* MR-1: structures, functions and opportunities. *J R Soc*
513 *Interface* **12** (2015).
514 11 El-Naggar, M. Y. & Finkel, S. E. Live Wires. *Scientist* **27**, 38-43 (2013).
515 12 Hartshorne, R. S. *et al.* Characterization of an electron conduit between bacteria
516 and the extracellular environment. *P Natl Acad Sci USA* **106**, 22169-22174
517 (2009).
518 13 Richardson, D. J. *et al.* The porin-cytochrome' model for microbe-to-mineral
519 electron transfer. *Mol Microbiol* **85**, 201-212 (2012).
520 14 White, G. F. *et al.* Rapid electron exchange between surface-exposed bacterial
521 cytochromes and Fe(III) minerals. *P Natl Acad Sci USA* **110**, 6346-6351 (2013).
522 15 Okamoto, A., Hashimoto, K., Nealson, K. H. & Nakamura, R. Rate enhancement
523 of bacterial extracellular electron transport involves bound flavin semiquinones. *P*
524 *Natl Acad Sci USA* **110**, 7856-7861, doi:Doi 10.1073/Pnas.1220823110 (2013).
525 16 Edwards, M. J. *et al.* Redox Linked Flavin Sites in Extracellular Decaheme
526 Proteins Involved in Microbe-Mineral Electron Transfer. *Sci. Rep.* **5** (2015).
527 17 Xu, S., Jangir, Y. & El-Naggar, M. Y. Disentangling the roles of free and
528 cytochrome-bound flavins in extracellular electron transport from *Shewanella*
529 *oneidensis* MR-1. *Electrochim Acta* **198**, 49-55 (2016).
530 18 Marsili, E. *et al.* *Shewanella* Secretes flavins that mediate extracellular electron
531 transfer. *P Natl Acad Sci USA* **105**, 3968-3973 (2008).
532 19 Coursolle, D., Baron, D. B., Bond, D. R. & Gralnick, J. A. The Mtr Respiratory
533 Pathway Is Essential for Reducing Flavins and Electrodes in *Shewanella*
534 *oneidensis*. *J Bacteriol* **192**, 467-474 (2010).
535 20 Gorby, Y. A. *et al.* Electrically conductive bacterial nanowires produced by
536 *Shewanella oneidensis* strain MR-1 and other microorganisms. *P Natl Acad Sci*
537 *USA* **103**, 11358-11363 (2006).
538 21 El-Naggar, M. Y. *et al.* Electrical transport along bacterial nanowires from
539 *Shewanella oneidensis* MR-1. *Proceedings of the National Academy of Sciences*
540 **107**, 18127-18131 (2010).
541 22 Pirbadian, S. *et al.* *Shewanella oneidensis* MR-1 nanowires are outer membrane
542 and periplasmic extensions of the extracellular electron transport components. *P*
543 *Natl Acad Sci USA* **111**, 12883-12888 (2014).
544 23 Ray, R., Lizewski, S., Fitzgerald, L. A., Little, B. & Ringeisen, B. R. Methods for
545 imaging *Shewanella oneidensis* MR-1 nanofilaments. *J Microbiol Meth* **82**, 187-
546 191 (2010).

- 547 24 Dohnalkova, A. C. *et al.* Imaging Hydrated Microbial Extracellular Polymers:
548 Comparative Analysis by Electron Microscopy. *Appl Environ Microb* **77**, 1254-
549 1262 (2011).
- 550 25 Gan, L. & Jensen, G. J. Electron tomography of cells. *Q Rev Biophys* **45**, 27-56,
551 doi:10.1017/S0033583511000102 (2012).
- 552 26 Pirbadian, S. & El-Naggar, M. Y. Multistep hopping and extracellular charge
553 transfer in microbial redox chains. *Physical Chemistry Chemical Physics* **14**,
554 13802-13808 (2012).
- 555 27 Polizzi, N. F., Skourtis, S. S. & Beratan, D. N. Physical constraints on charge
556 transport through bacterial nanowires. *Faraday Discuss* **155**, 43-62 (2012).
- 557 28 Gorby, Y. *et al.* Redox-reactive membrane vesicles produced by *Shewanella*.
558 *Geobiology* **6**, 232-241 (2008).
- 559 29 Kuehn, M. J. & Kesty, N. C. Bacterial outer membrane vesicles and the host-
560 pathogen interaction. *Genes Dev* **19**, 2645-2655, doi:10.1101/gad.1299905
561 (2005).
- 562 30 Firer-Sherwood, M. A., Ando, N., Drennan, C. L. & Elliott, S. J. Solution-based
563 structural analysis of the decaheme cytochrome, MtrA, by small-angle X-ray
564 scattering and analytical ultracentrifugation. *J Phys Chem B* **115**, 11208-11214,
565 doi:10.1021/jp203603r (2011).
- 566 31 Shetty, A., Chen, S., Tocheva, E. I., Jensen, G. J. & Hickey, W. J. Nanopods: a
567 new bacterial structure and mechanism for deployment of outer membrane
568 vesicles. *PLoS One* **6**, e20725, doi:10.1371/journal.pone.0020725 (2011).
- 569 32 McCaig, W. D., Koller, A. & Thanassi, D. G. Production of outer membrane
570 vesicles and outer membrane tubes by *Francisella novicida*. *J Bacteriol* **195**,
571 1120-1132, doi:10.1128/JB.02007-12 (2013).
- 572 33 Wanner, G., Vogl, K. & Overmann, J. Ultrastructural characterization of the
573 prokaryotic symbiosis in "*Chlorochromatium aggregatum*". *J Bacteriol* **190**,
574 3721-3730, doi:10.1128/JB.00027-08 (2008).
- 575 34 Galkina, S. I. *et al.* Membrane tubules attach *Salmonella Typhimurium* to
576 eukaryotic cells and bacteria. *FEMS Immunol Med Microbiol* **61**, 114-124,
577 doi:10.1111/j.1574-695X.2010.00754.x (2011).
- 578 35 Pande, S. *et al.* Metabolic cross-feeding via intercellular nanotubes among
579 bacteria. *Nat Commun* **6**, 6238, doi:10.1038/ncomms7238 (2015).
- 580 36 Benomar, S. *et al.* Nutritional stress induces exchange of cell material and
581 energetic coupling between bacterial species. *Nat Commun* **6**, 6283,
582 doi:10.1038/ncomms7283 (2015).
- 583 37 Bohuszewicz, O., Liu, J. & Low, H. H. Membrane remodelling in bacteria. *J*
584 *Struct Biol* **196**, 3-14, doi:10.1016/j.jsb.2016.05.010 (2016).
- 585 38 Pérez-Cruz, C. *et al.* New type of outer membrane vesicle produced by the Gram-
586 negative bacterium *Shewanella vesiculosa* M7T: implications for DNA content.
587 *Appl Environ Microbiol* **79**, 1874-1881, doi:10.1128/AEM.03657-12 (2013).
- 588 39 Remis, J. P. *et al.* Bacterial social networks: structure and composition of
589 *Myxococcus xanthus* outer membrane vesicle chains. *Environ Microbiol* **16**, 598-
590 610, doi:10.1111/1462-2920.12187 (2014).

591 40 Wei, X., Vassallo, C. N., Pathak, D. T. & Wall, D. Myxobacteria produce outer
592 membrane-enclosed tubes in unstructured environments. *J Bacteriol* **196**, 1807-
593 1814, doi:10.1128/JB.00850-13 (2014).

594 41 Dubey, G. P. *et al.* Architecture and Characteristics of Bacterial Nanotubes. *Dev*
595 *Cell* **36**, 453-461, doi:10.1016/j.devcel.2016.01.013 (2016).

596 42 Bar-Ziv, R. & Moses, E. Instability and "pearling" states produced in tubular
597 membranes by competition of curvature and tension. *Phys Rev Lett* **73**, 1392-
598 1395, doi:10.1103/PhysRevLett.73.1392 (1994).

599 43 Bar-Ziv, R., Tlusty, T. & Moses, E. Critical dynamics in the pearling instability of
600 membranes. *Physical Review Letters* **79**, 1158-1161,
601 doi:10.1103/PhysRevLett.79.1158 (1997).

602 44 Sanborn, J., Oglecka, K., Kraut, R. S. & Parikh, A. N. Transient pearling and
603 vesiculation of membrane tubes under osmotic gradients. *Faraday Discuss* **161**,
604 167-176; discussion 273-303 (2013).

605 45 Kantsler, V., Segre, E. & Steinberg, V. Critical dynamics of vesicle stretching
606 transition in elongational flow. *Phys Rev Lett* **101**, 048101,
607 doi:10.1103/PhysRevLett.101.048101 (2008).

608 46 Sinha, K., Gadkari, S. & Thaokar, R. Electric field induced pearling instability in
609 cylindrical vesicles. *Soft Matter* **9**, 7274-7293, doi:10.1039/c3sm00052d (2013).

610 47 Chaieb, S. & Rica, S. Spontaneous curvature-induced pearling instability.
611 *Physical Review E* **58**, 7733-7737, doi:10.1103/PhysRevE.58.7733 (1998).

612 48 Yu, Y. & Granick, S. Pearling of Lipid Vesicles Induced by Nanoparticles.
613 *Journal of the American Chemical Society* **131**, 14158+, doi:10.1021/ja905900h
614 (2009).

615 49 Tsafrir, I. *et al.* Pearling instabilities of membrane tubes with anchored polymers.
616 *Physical Review Letters* **86**, 1138-1141, doi:10.1103/PhysRevLett.86.1138
617 (2001).

618 50 Campelo, F. & Hernandez-Machado, A. Model for curvature-driven pearling
619 instability in membranes. *Physical Review Letters* **99**,
620 doi:10.1103/PhysRevLett.99.088101 (2007).

621 51 Breuer, M., Rosso, K. M. & Blumberger, J. Electron flow in multiheme bacterial
622 cytochromes is a balancing act between heme electronic interaction and redox
623 potentials. *Proc Natl Acad Sci U S A* **111**, 611-616, doi:10.1073/pnas.1316156111
624 (2014).

625 52 Byun, H. S., Pirbadian, S., Nakano, A., Shi, L. & El-Naggar, M. Y. Kinetic Monte
626 Carlo Simulations and Molecular Conductance Measurements of the Bacterial
627 Decaheme Cytochrome MtrF. *Chemelectrochem* **1**, 1932-1939,
628 doi:10.1002/celc.201402211 (2014).

629 53 Ross, D. E. *et al.* Characterization of protein-protein interactions involved in iron
630 reduction by *Shewanella oneidensis* MR-1. *Appl Environ Microbiol* **73**, 5797-
631 5808, doi:10.1128/AEM.00146-07 (2007).

632 54 Dong, H. *et al.* Structural basis for outer membrane lipopolysaccharide insertion.
633 *Nature* **511**, 52-56, doi:10.1038/nature13464 (2014).

634 55 Poole, R. K. *Advances in Bacterial Electron Transport Systems and Their*
635 *Regulation*. 1st edn, p. 103 (Academic Press, 2016).

636 56 Paquete, C. M. *et al.* Exploring the molecular mechanisms of electron shuttling
637 across the microbe/metal space. *Front Microbiol* **5**, 318,
638 doi:10.3389/fmicb.2014.00318 (2014).
639 57 Ramadurai, S. *et al.* Lateral diffusion of membrane proteins. *J Am Chem Soc* **131**,
640 12650-12656, doi:10.1021/ja902853g (2009).
641 58 Cornejo, E., Subramanian, P., Li, Z., Jensen, G. J. & Komeili, A. Dynamic
642 Remodeling of the Magnetosome Membrane Is Triggered by the Initiation of
643 Biomineralization. *MBio* **7**, e01898-01815, doi:10.1128/mBio.01898-15 (2016).
644 59 Zheng, S. Q. *et al.* UCSF tomography: an integrated software suite for real-time
645 electron microscopic tomographic data collection, alignment, and reconstruction.
646 *J Struct Biol* **157**, 138-147, doi:10.1016/j.jsb.2006.06.005 (2007).
647 60 Kremer, J. R., Mastronarde, D. N. & McIntosh, J. R. Computer visualization of
648 three-dimensional image data using IMOD. *J Struct Biol* **116**, 71-76,
649 doi:10.1006/jsbi.1996.0013 (1996).
650 61 Pettersen, E. F. *et al.* UCSF Chimera--a visualization system for exploratory
651 research and analysis. *J Comput Chem* **25**, 1605-1612, doi:10.1002/jcc.20084
652 (2004).
653 62 The PyMOL Molecular Graphics System, Version 1.7.2.0 Schrodinger, LLC.
654 63 Hardt, S. L. Rates of diffusion controlled reactions in one, two and three
655 dimensions. *Biophys Chem* **10**, 239-243 (1979).
656 64 Hardt, S. L. The Diffusion Transit Time; A Simple Derivation. *Bulletin of*
657 *Mathematical Biology* **43**, 89-99, doi:10.1007/BF02460942 (1981).
658

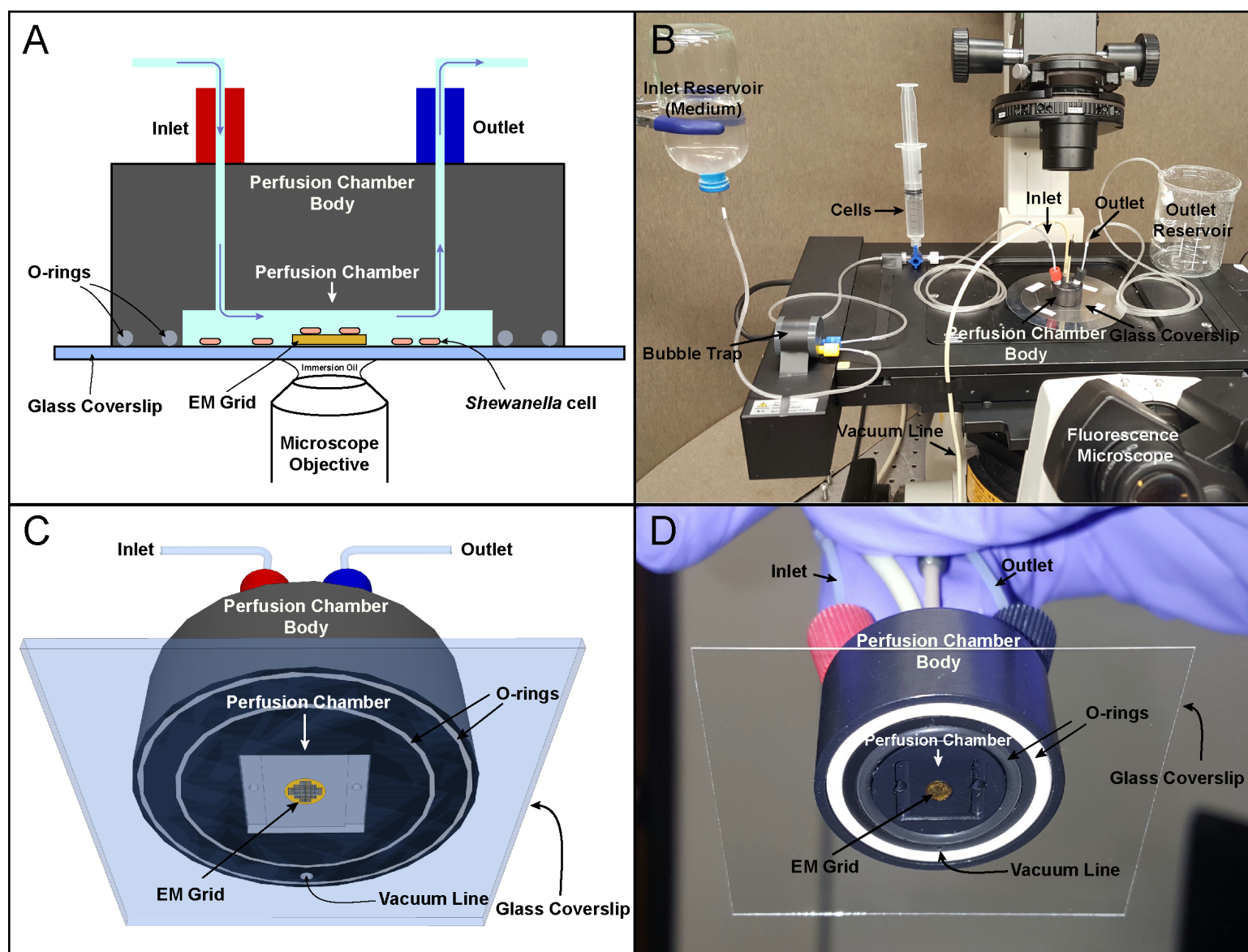


Fig. 1: Schematic and actual images of the perfusion flow imaging platform (objects not drawn to scale). (A) Cross-sectional and (B) Three-dimensional (3D) views of the perfusion flow imaging platform. An electron microscopy (EM) grid is glued to a glass coverslip that seals the perfusion chamber. *S. oneidensis* cells injected into the sealed chamber attach to the grid surface and are sustained by a continuous flow of the medium. Cells are labeled with the fluorescent membrane dye FM 4-64FX and monitored real-time for nanowire growth using an inverted fluorescent microscope placed under the perfusion chamber. (C) 3D schematic and (D) Image of the perfusion chamber interior with an attached EM grid.

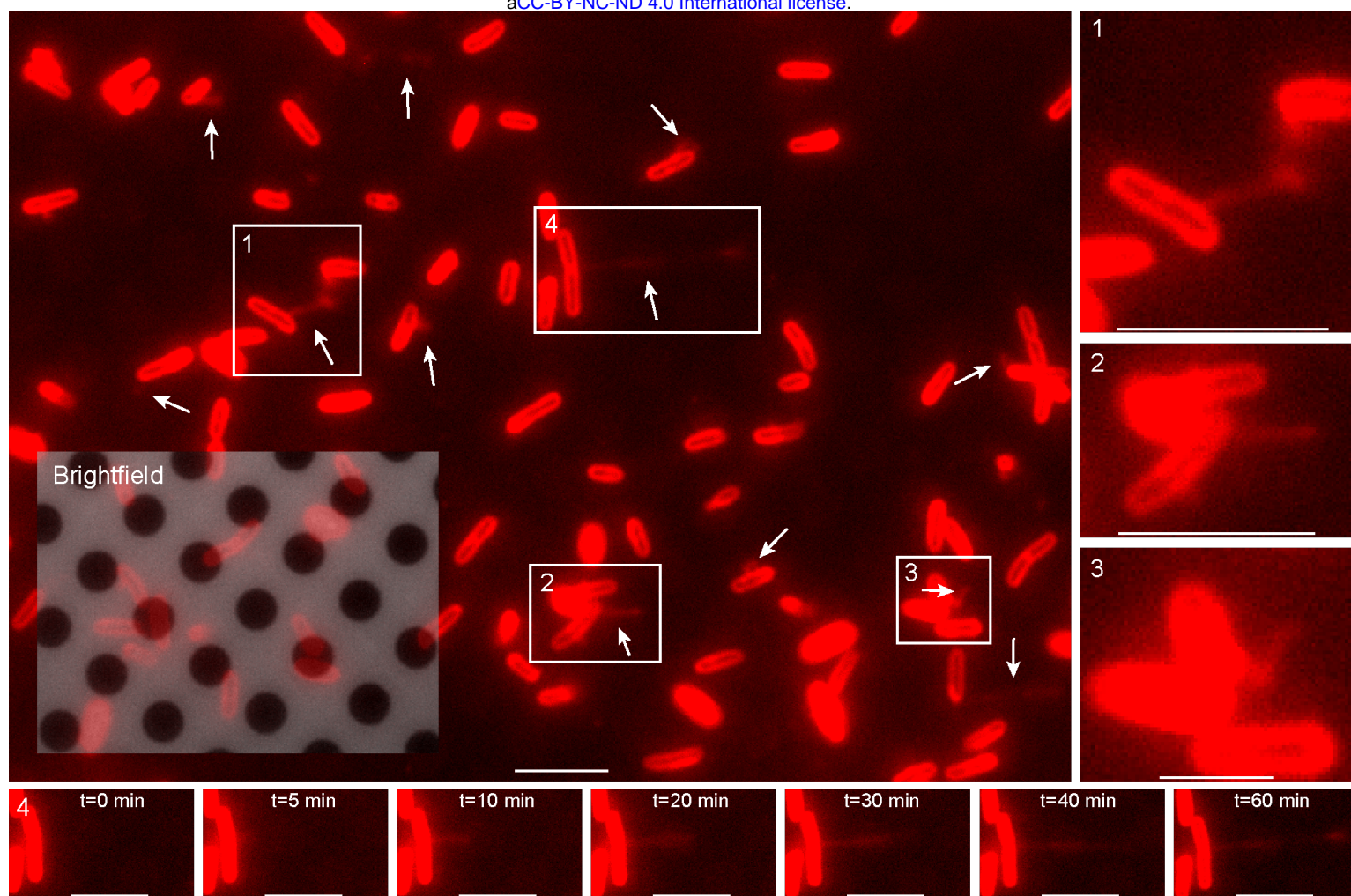


Fig. 2: Live *in vivo* observation of the formation of *S. oneidensis* nanowires (white arrows) on an EM grid (Scale bar: 5 μ m). Inset is an overlap of red fluorescence and reflective brightfield channels, revealing both the holey carbon film coating the EM grid and the fluorescently labeled cells attached to it. Movie S3 is a time-lapse movie of this figure. (1, 2, and 3) Enlarged views of boxed regions from the main panel. (Scale bars in 1, 2, and 3: 5, 5, and 2 μ m, respectively). (4) Time-lapse images of the growth of a single nanowire from boxed region 4 in the main panel. $t=0$ min is an arbitrary starting timepoint. (Scale bars: 5 μ m).

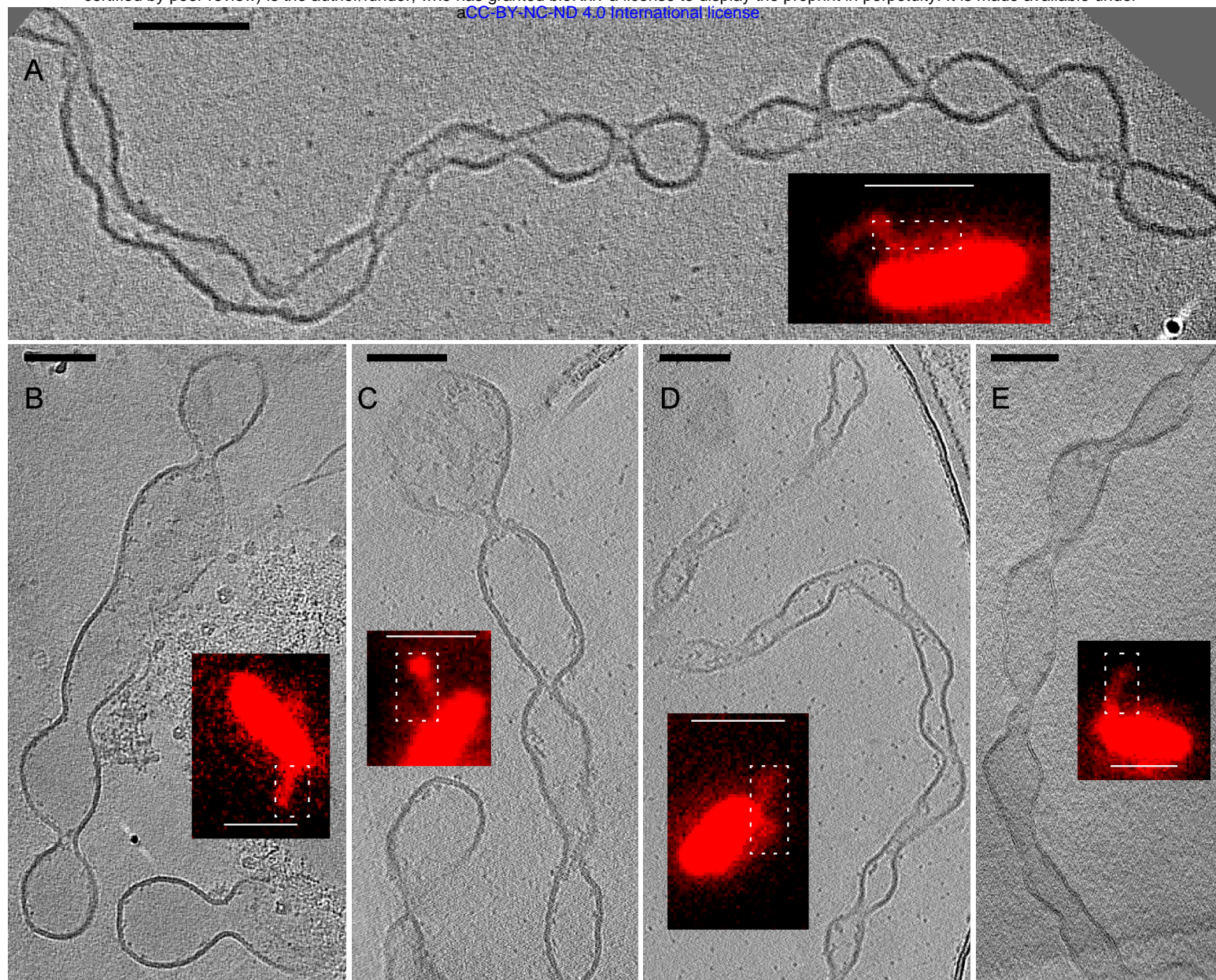


Fig. 3: Targeting dynamic nanowire structures of *S. oneidensis* for ECT using Correlative Light and Electron Microscopy (CLEM). To visualize the structure of nanowires by ECT, target locations on fixed and plunge-frozen EM grids, from the perfusion flow imaging platform, were imaged, revealing the OMV chain morphology of the nanowires. (A, B, C, D, and E) Representative images from ECT, with corresponding fluorescent light microscopy image insets. (ECT scale bars: 100 nm, fLM scale bars: 2 μ m). White dotted boxes in the fLM images indicate the corresponding approximate regions imaged in ECT. The ECT images shown are tomographic slices from three-dimensional reconstructions. See also Fig. S5 and Movies S1 and S2.

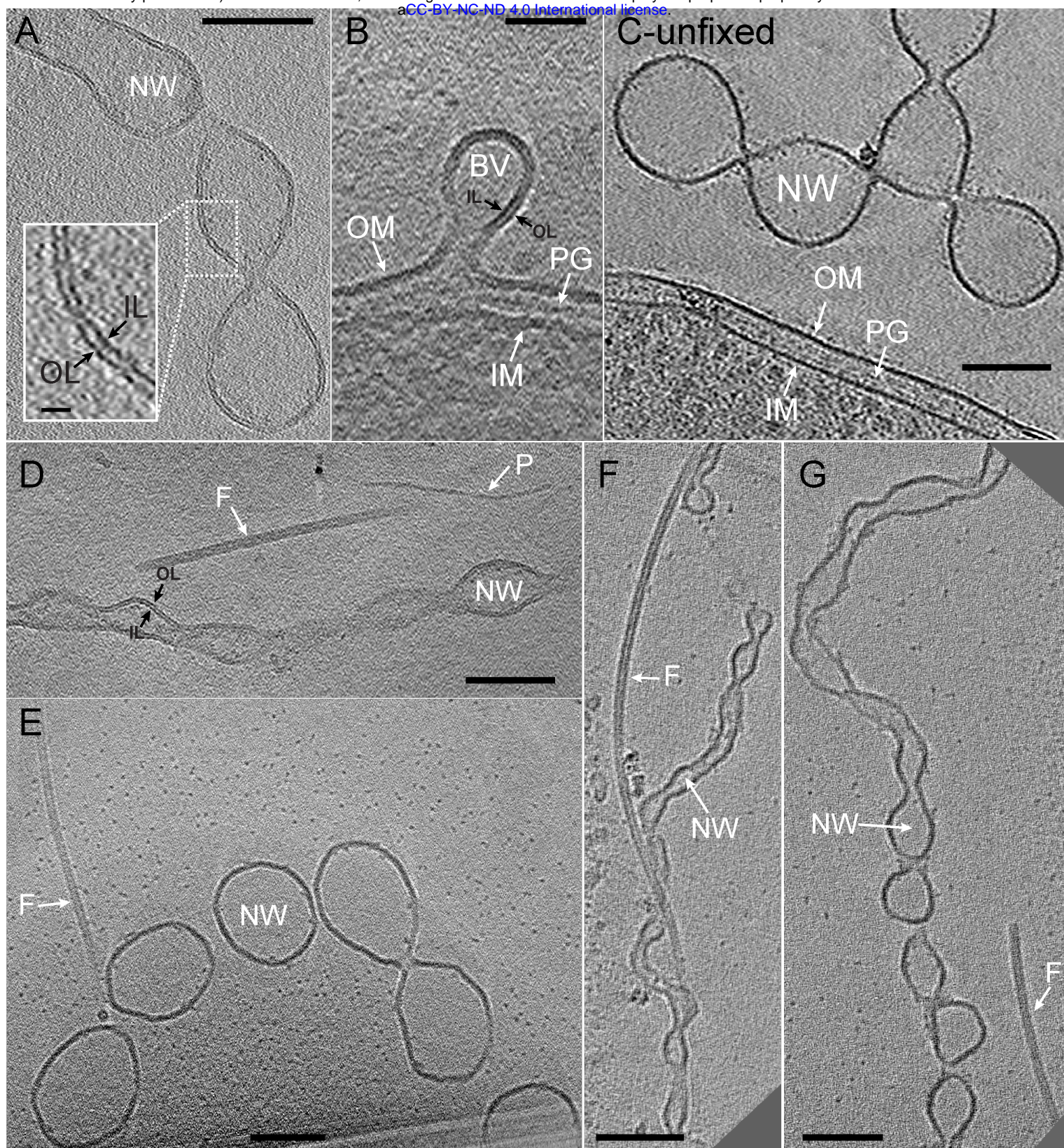


Fig. 4: Electron cryo-tomography (ECT) images of *S. oneidensis* nanowires. (A) Nanowire membrane bilayer is clearly resolved. Inset is enlarged view of boxed region with the inner and outer leaflets indicated with arrows. (Scale bar: 100 nm, inset scale bar: 10 nm). (B) A budding vesicle (BV) emerging as

an extension of the cellular outer membrane. A similar process perhaps underlies the initial stages of nanowire formation. (Scale bar: 50 nm). (C) Nanowire from an unfixed chemostat sample exhibits identically branched OMV chain morphology as observed in both unfixed and fixed samples from the perfusion flow imaging platform. (Scale bar: 100 nm). See also Figs. S4, S9 and Movie S12. (D) A nanowire, a flagellum and a pilus next to each other allowing direct comparison of their sizes and morphologies, indicating that ECT facilitates the identification and distinguishability of different extracellular appendages in *S. oneidensis*. (Scale bar: 100 nm). See also Movie S4. (E, F, and G) ECT reveals nanowires are of varying thicknesses and degrees of tubulation. Next to each nanowire is a flagellum that can act as a molecular marker for comparison of varying nanowire dimensions. (Scale bars: 100 nm). See also Movie S5 corresponding to (F). NW-nanowire, F-flagellum, P-pilus, BV-budding vesicle, OM-outer membrane, IM-inner membrane, PG-peptidoglycan, OL-outer leaflet, IL-inner leaflet.

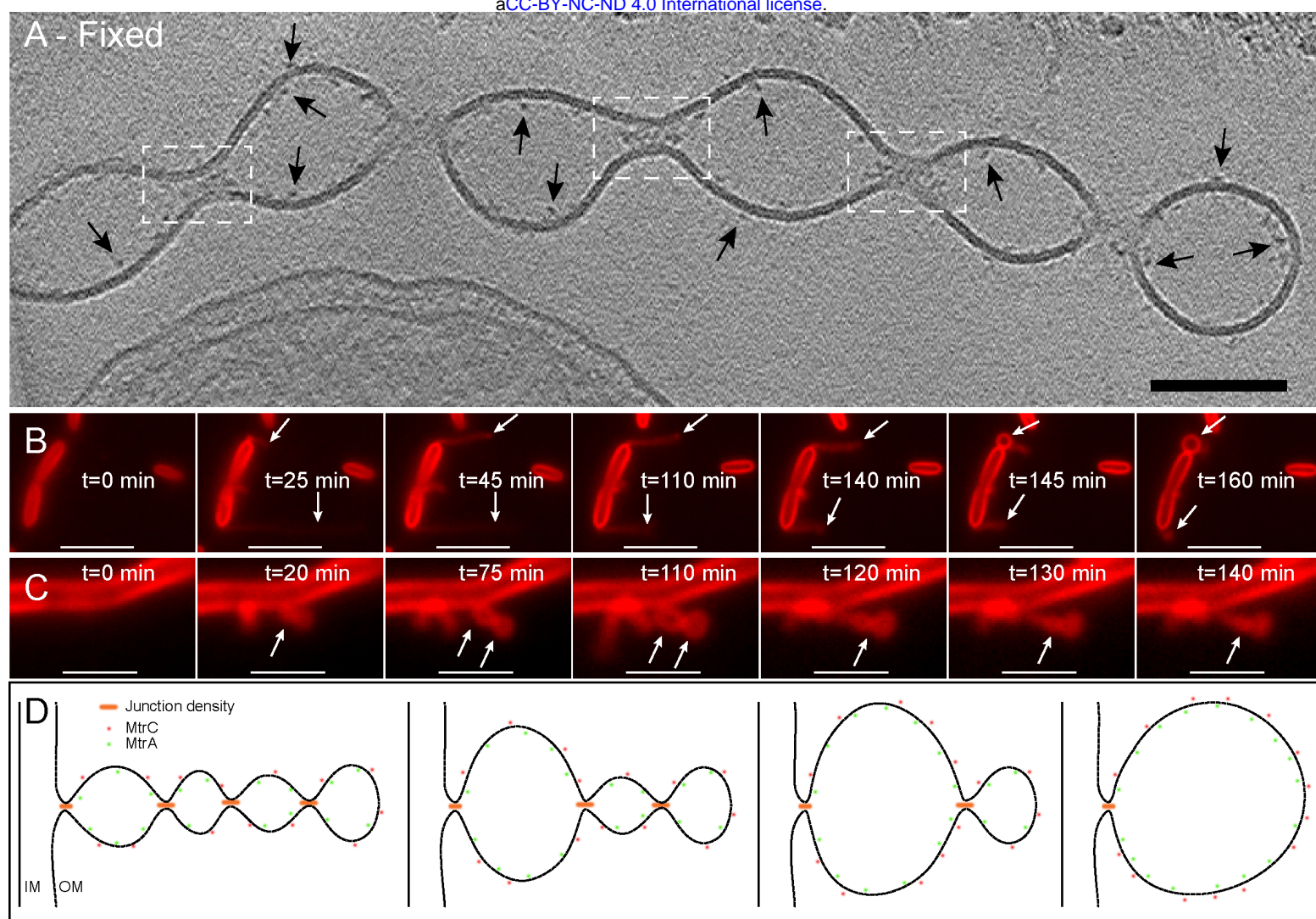


Fig. 5: Proposed model for the formation and stabilization of OMV chains. (A) ECT image of a chemically fixed nanowire reveals the presence of densities at junctions that connect one vesicle to the next along the OMV chain (white dashed boxes). All densities are not visible in the tomographic slice in (A), while Movie S6 is a 3D reconstruction revealing the densities present at every junction. In addition, densities possibly related to decaheme cytochromes can be observed on the interior and exterior of the outer membrane along the nanowire (arrows). (Scale bar: 100 nm). See also Fig. S7. (B and C) Time-lapse fluorescence images recorded real-time in the perfusion flow imaging platform monitoring the growth and transformation of a nanowire from (B) An apparently long filament (OMV chain morphology) to a single large vesicle (indicated by arrows) in *S. oneidensis* Δflg (a mutant strain lacking flagellin

genes). (See also Movie S7). (Note that nanowires from wild-type cells also exhibit a similar behavior as shown in Movie S8) and (C) A large vesicular morphology to an apparently smoother filament (OMV chain morphology) (indicated by arrows) in wild-type *S. oneidensis* MR-1 cells. See also Movies S9 and S10. The cells and the nanowires in (B) and (C) are stained by the membrane stain FM 4-64FX. (Scale bars in B and C: 5 and 2 μm , respectively). (D) Schematic depicting a hypothesis for the formation and stabilization mechanism of OMV chains: Junction densities on the interior of the nanowire facilitate the constriction of the membrane, enabling the formation of an OMV chain. These constriction densities can be removed or added to facilitate transformation of an OMV chain to a large vesicle or vice versa as observed in (B) and (C) respectively.

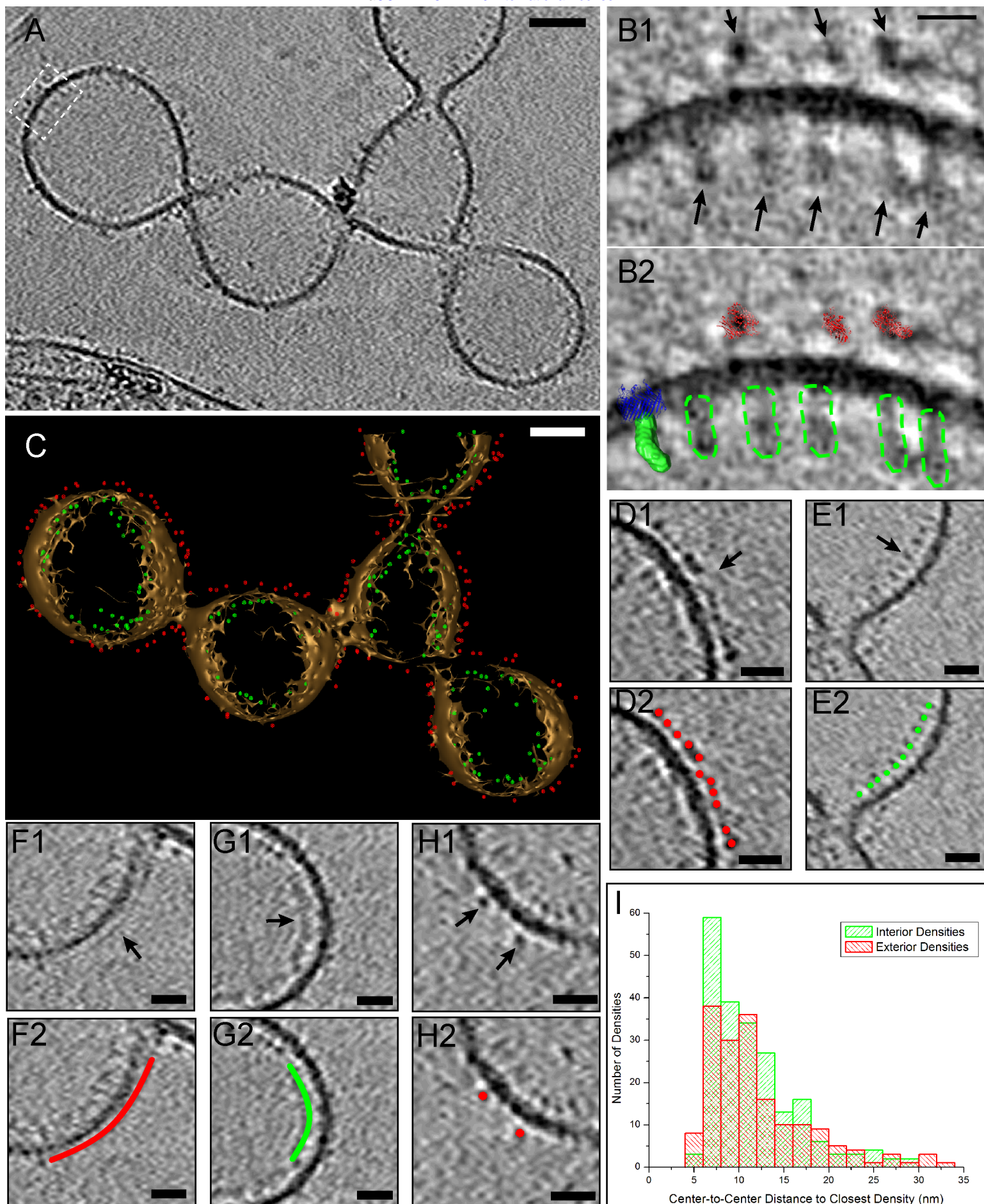


Fig. 6: Positions and packing of decaheme cytochromes along the nanowire length in *S. oneidensis* (A) ECT image of an unfixed nanowire showing densities on both the interior and exterior of the outer membrane corresponding to putative MtrA and MtrC cytochromes respectively (Scale bar: 50 nm). (B1) Enlarged view of boxed area from (A). (B2) Comparison of EM densities in (B1) with the crystal structure of MtrC, low resolution SAXS model of MtrA, and the MtrB homolog LptD (only the LptD structure was used for this model from the LptD-LptE two-protein crystal structure), highlighting the similarity in overall shape and size of these structures to the observed EM densities. Red: MtrC crystal structure, Green: surface view of MtrA SAXS model, Blue: LptD crystal structure, Dotted green: outline of putative MtrA densities on the EM map. (Scale bar: 10 nm). (C) 3D isosurface view of the nanowire in (A) with all the interior and exterior densities (putative MtrA and MtrC respectively) represented as model points in green and red respectively. (Scale bar: 50 nm). See also Movie S11. (D-G) Representative regions from the nanowire in (A) demonstrating differences in packing density of MtrA and MtrC. (D1) Relatively closely packed exterior densities of putative MtrC with an average center-to-center inter-density distance of 7.3 nm (SD=2.1 nm). (E1) Relatively closely packed interior densities of putative MtrA with an average center-to-center inter-density distance of 8.9 nm (SD=2.0 nm). Continuous (F1) interior and (G1) exterior densities that may be related to tightly packed MtrA and MtrC respectively. (H1) Isolated exterior densities of putative MtrC. (D2), (E2), (F2), (G2), and (H2) are duplicates of (D1), (E1), (F1), (G1), and (H1) respectively, with model points or lines highlighting the interior (green) and exterior (red) densities. (I) Histogram showing distribution of center-to-center distances of all putative MtrAs (in green) and MtrCs (in red).